SAND 2000-1771J

RECEIVED
AUG 17 2000
OSTI

3–D Finite Element Analysis of Induction Logging in a Dipping Formation

Mark E. Everett
Department of Geology and Geophysics, Texas A&M University
College Station, TX, 77843

Eugene A. Badea
Department of Electrical Engineering, University of Houston
Houston, TX, 77204-4793

Liang C. Shen
Department of Electrical Engineering, University of Houston
Houston, TX, 77204-4793

Gulamabbas A. Merchant
Multiphysics Numerical Research Group
16011 Mission Village Dr., Houston, TX, 77083

Chester J. Weiss
Geophysical Technology ~~Division~~ Dept, Sandia National Laborator~~y~~ies
P.O.Box 5800, Albuquerque, NM, 87185

Submitted to IEEE Transactions on Antennas and Propagation

June 13, 2000

DISCLAIMER

Abstract

Electromagnetic induction by a magnetic dipole located above a dipping interface is of relevance to the petroleum well–logging industry. The problem is fully three–dimensional (3–D) when formulated as above, but reduces to an analytically tractable one–dimensional (1–D) problem when cast as a small tilted coil above a horizontal interface. The two problems are related by a simple coordinate rotation. An examination of the induced eddy currents and the electric charge accumulation at the interface help to explain the inductive and polarization effects commonly observed in induction logs from dipping geological formations. The equivalence between the 1–D and 3–D formulations of the problem enables the validation of a previously published finite element solver for 3–D controlled–source electromagnetic induction.

Introduction

Wireline induction logging is a controlled–source electromagnetic (CSEM) application that utilizes coaxial borehole transmitter and receiver coils of fixed separation. The method is widely used within the oil industry to determine electrical conductivity depth profiles within sedimentary formations. Spatial variations in electrical conductivity are analyzed jointly with other physical properties derived from well logs to discriminate between water, shale and hydrocarbon–bearing rocks.

An induction log reflects to a certain extent the true formation electrical conductivity, but logs are contaminated by electromagnetic (EM) induction effects associated with the presence of the borehole, bed boundaries, the dip of the formation bedding planes with respect to the borehole axis, formation anisotropy, tool eccentricity, and the fluid invasion zone. Fully 3–D numerical simulations are required to model these effects and eventually permit an estimation of the true formation conductivity profile from the observed log response.

The effect of dip on induction log responses has long been of interest to the oil industry. Dip is defined as the angle α between the borehole/tool axis and the normal to the bedding planes. An early deconvolution technique [1] was developed to correct induction logs for the dip effect in formations without fluid invasion. The technique is based on the assumption that the log response (apparent conductivity) can be regarded as a linear function of the true formation conductivity. The linearity assumption is reasonable for modest conductivity values within beds but it breaks down near bed boundaries due to the nonlinear EM effects of electric charge accumulation. The charge accumulates as eddy currents generated by the tilted dipole are forced across the interface.

A 3–D investigation of the charge accumulation effects on induction logs for the case of dip with invasion was carried out in [2] using an extended Born approximation. More recent studies of the dip–with–invasion induction logging problem use finite difference (FD) and integral equation methods [3–5]. The emphasis in these studies is typically on code validation and investigation of dip/invasion effects as they pertain to industry–standard logging tool responses. However, to properly interpret induction logging responses it is necessary to have a good understanding of the underlying EM field behavior.

The objective of this study is to analyze the physics of electromagnetic diffusion generated by a dipole transmitter embedded in a dipping formation without a borehole. The problem is one–dimensional if the vertical axis coincides with the normal to the bed boundary. All the beds are assumed to be homogeneous. In this case, an analytic solution is available [6], which is expressed by the superposed fields of a vertical and horizontal magnetic dipole exciting a horizontally layered formation. The problem, however, is fully 3–D when solved in a coordinate system in which the vertical axis is aligned with the dipole moment vector. Most 3–D numerical solutions [3–5,8] operate in this coordinate system. Therefore, the 1–D analytic solution can be used to help validate 3–D numerical results.

In this study, a finite element (FE) algorithm based on the $(\mathbf{A}_s, \Psi_s)$ secondary coupled electromagnetic potentials formulation of Maxwell's equations [7–8] is used, where $\mathbf{A}_s$ is a secondary magnetic vector potential and Ψ_s is a secondary electric scalar potential. The secondary potentials are defined relative to primary potentials $(\mathbf{A}_p, \Psi_p)$ that are known solutions to a specified CSEM induction problem. The method operates with unstructured meshes and consequently can address difficult EM induction problems characterized by complicated conductor geometries.

Governing Equations

In source–free regions, the governing equations for the Coulomb–gauged coupled potential formulation of Maxwell's equations assuming $e^{-i\omega t}$ harmonic excitation are given by [8]:

$$\nabla \times \nabla \times \mathbf{A} - \nabla(\nabla \cdot \mathbf{A}) - j\omega\mu_0\sigma(\mathbf{A} + \nabla\Psi) = 0 \tag{1}$$

$$\nabla \cdot [j\omega\mu_0\sigma(\mathbf{A} + \nabla\Psi)] = 0. \tag{2}$$

Numerical solutions are best obtained in terms of secondary potentials $(\mathbf{A}_\mathrm{S}, \Psi_\mathrm{S})$ defined by: $\mathbf{A}$=$\mathbf{A}_\mathrm{P}$ +$\mathbf{A}_\mathrm{S}$ and Ψ=Ψ_S+ Ψ_P. The governing equations become:

$$\nabla \times (\nabla \times \mathbf{A}_\mathrm{S}) - \nabla(\nabla \cdot \mathbf{A}_\mathrm{S}) - i\omega\mu_0\sigma(\mathbf{A}_\mathrm{S} + \nabla\Psi_S) = j\omega\mu_0\Delta\sigma(\mathbf{A}_\mathrm{P} + \nabla\Psi_\mathrm{P}) \tag{3}$$

$$\nabla \cdot [i\omega\mu_0\sigma(\mathbf{A}_\mathrm{S} + \nabla\Psi_\mathrm{S})] = -\nabla \cdot [j\omega\mu_0\sigma(\mathbf{A}_\mathrm{P} + \nabla\Psi_\mathrm{P})]\,, \tag{4}$$

where $\Delta\sigma \equiv \sigma - \sigma_0$ is the difference between two conductivity distributions: $\sigma(\mathbf{r})$, the actual conductivity whose response is required, and $\sigma_0(\mathbf{r})$, a 'background' conductivity whose response is already known. The differential equations for $(\mathbf{A}_\mathrm{S}, \Psi_\mathrm{S})$ are solved using the finite element method. The boundary conditions are of homogeneous Dirichlet type [8].

For the primary potentials $(\mathbf{A}_\mathrm{P}, \Psi_\mathrm{P})$ we consider the solution for a horizontal loop of radius a, placed at z=z_0 and carrying current I, which is embedded in a conducting wholespace of uniform conductivity σ_0. The formula for $\mathbf{A}_P$ in cylindrical coordinates is:

$$\mathbf{A}_\mathrm{P} = \frac{\mu_0 I a \hat{\phi}}{2} \int_0^\infty \frac{1}{\alpha_0} e^{-\alpha_0|z-z_0|} J_1(\lambda a)\, J_1(\lambda\rho)\, \lambda d\lambda \tag{5}$$

where $\alpha_0^2 = \lambda^2 - j\mu_0\omega\sigma_0$, while Ψ_P vanishes in this case. The Hankel transform is performed using a digital filter method [9].

Method

A derivation of the sparse, complex symmetric linear system of equations that is generated by applying the finite element method to the $(\mathbf{A}_S, \Psi_S)$ partial differential equations is provided in the Appendix. The linear system is solved using the quasi–minimal residual (QMR) method described in [10]. Jacobi preconditioning is used to enhance the convergence rate of the QMR iterates [11].

The solution domain Ω is discretized into tetrahedra using a mesh generator with local refinement capability [8,12]. The mesh generator produces high–quality tetrahedra with few if any long, thin ones that degrade the accuracy of the FE solution. Local mesh refinement is performed in regions where electromagnetic field gradients are expected to be large, such as along bed boundaries, or where high accuracy is required, such as close to receivers. The local refinment algorithm allows multiple nested refinements so that a mesh that has been locally refined can be further refined within the same region. An example of a mesh with two nested local refinements is given in Figure 1.

Once the mesh is generated and the finite element linear system solved, a moving least squares interpolation (MLSI) method [13] is used to differentiate the computed potentials and hence obtain the direct electromagnetic field components at any specified point within the solution domain.

Benchmark

The problem considered is that of a horizontal coil embedded in a double halfspace electrically conducting medium with a dipping interface. The geometry is illustrated in Figure 2, in the coordinate system used by the FE solution. In the coord~~inate system chosen for the analytic~~ solution, the coil is tilted and the interface is horizontal. However, the FE and analytic solutions are equivalent once the proper coordinate transformation has been applied, with both containing the full 3–D physics of charge accumulation at the interface.

The analytic solution is the superposition of a horizontal magnetic dipole (HMD) and a vertical magnetic dipole (VMD) energizing a double half–space formation with a horizontal interface. A conventional logging tool measures the component of magnetic field that is aligned with the transmitter axis. Therefore, in the coordinate system used by the FE method, the magnetic field sensed by the logging tool is given by $H_{\rm RX} = H_z$, whereas for the analytic solution, it is

$$H_{\rm RX} = sin^2\alpha H_x^{\rm HMD} + sin\alpha\, cos\alpha\, [H_x^{\rm VMD} + H_z^{\rm HMD}] + cos^2\alpha H_z^{\rm VMD}, \tag{6}$$

where $H_x^{\rm VMD}$ is the x–component of the magnetic field generated by the VMD source of the same magnetic moment as the transmitter, and so forth.

The FE calculations were performed in terms of secondary potentials, where the primary potential $\mathbf{A}_p$ is that due to a horizontal loop energizing a uniformly conducting wholespace of conductivity σ_0, which is the value characterizing the bed in which the transmitter is located. The MLSI algorithm was then applied to extract the secondary magnetic field.

A mesh (60k nodes, 300k tetrahedra) was constructed using three nested refinements in the region where the vertical (coil) axis intersects the interface between upper and lower halfspaces, as shown by the shaded rectangle in Fig.2. A linear transformation of the form

$$z_i \leftarrow z_i + x_i \tan\alpha \tag{7}$$

is applied to each node i=1,...,N of the mesh to ensure that the edges of the tetrahedra conformed to both the coil axis and to the dipping material interface, see the example in Figure 3. Dip angles of 30°, 45° and 60° are considered. The parameters used in this study are σ_0=0.1 S/m, σ_1=1.0 S/m. Convergence of the QMR solver was achieved in about 800–2000 iterations, the slower rate of convergence corresponding to higher dip angles.

The secondary magnetic field components H_{sx} (hereafter called the X–signal) and H_{sz} (the Z–signal) as a function of position along the coil axis are shown in Figure 4a–f for the various dip angles. The total Z–signal would be recorded for a single logging point by a tool consisting of one transmitter and a continuous array of aligned receivers. The total X–signal would be measured by tools whose receiver axes are oriented in the x–direction, orthogonal to the transmitter axis. The secondary X, Z–signals are plotted, rather than the total response, since they more clearly reveal the underlying physics of induction logging in a dipping formation.

In Figs.4a–f, the center of the transmitting coil is located a distance h=1.5 m below the material interface. The coil has radius of 0.01 m, and carries a 10^{10} A current oscillating at 2.5 MHz. The FE–computed responses (larger symbols) are compared to equivalent solutions (smaller symbols) using the Sandia National Labs 3–D FD code [11]. The analytic Z–signals are plotted (lines without symbols) as a reference.

A very good agreement for the tilt angles of 30° and 45° is found between the FE–computed and the FD–computed X–signal and Z–signal. At the highest tilt angle considered, α=60°, there is a larger disagreement, which can be attributed to the decrease in quality of the mesh tetrahedra. In Figure 5 the tetrahedron mean quality factor [12] is plotted versus the tilt angle, for both a mesh without local refinement and for the operational mesh containing the three nested refinements. As the tilt angle increases, the tetrahedra become progressively longer and thinner in order to simultaneously conform to both the z–axis and the dipping material interface. A long, thin tetrahedron has a very small quality factor, near zero, while a well-shaped tetrahedron has a quality factor between 0.6–1.0. A poor quality mesh containing many long, thin tetrahedra leads to a badly conditioned FE matrix and an accompanying loss of accuracy in the FE–computed EM responses.

It is also evident from Fig.5 that the refined mesh is of poorer overall quality than the unrefined mesh. This illustrates a trade-off involved in local mesh refinement: additional tetrahedra increase the accuracy of FE–computed solutions only if they are of sufficiently high quality. In the current version of the mesh generator, the quality of the tetrahedra in a specified region decreases with the number of times that the region is refined [8]. In view of these factors, the generation of high–quality, conforming meshes for large tilt angles and multiple nested refinements is an important component of our ongoing research.

Inductive and Polarization Effects

The real component Z–signals contain sharp peaks at the bed interface for high tilt angles, see Figs. 4d and 4f. These peaks are known as "polarization horns" in the well–logging industry and arise due to the combined effects of: (a) induced eddy currents, and; (b) currents that dissipate the charge accumulation at the material interface.

To understand the physics of induction by a tilted coil over a horizontal interface, it is instructive to examine the secondary fields that are generated by the constituent vertical and horizontal magnetic dipoles. A schematic representation of the induced eddy currents near the interface is shown in Figure 6 for the case of VMD excitation. The currents flow azimuthally in the x/y–plane. There is no vertical current flow, and hence no charge accumulation at the interface.

The physics of induction by the HMD source over a horizontal interface is more complicated. Assume the HMD source is located in the upper half–space. The induced eddy currents will resemble an image of the transmitter reflected in the lower medium. The eddy current pattern is shown in Figure 7. Notice that there is a vertical component to the current flow, and some of the currents leak into the upper medium (not shown in the figure), so that electric charges will accumulate on the interface. A schematic representation of the charge accumulation is shown in Figure 8.

Contours of the real secondary magnetic field due to the tilted coil (α=45°) are shown in Figure 9. The quantity plotted is the component aligned with the transmitter axis. The transmitter is located at position (0.0,1.5) on the plot. The coordinate system for the plot is the one for the analytic solution. The coil axis is drawn as a reference. The magnetic field distribution shown in the figure is generated by both the induced eddy currents and the dissipative currents previously discussed. Notice there is a kink in the contours close to location (-1.0,0.0). This kink corresponds to the sharp peak seen in Fig.4d.

Discussion

A very good agreement between analytic, FD and FE solutions has been achieved. The analytic solution is 1–D when the problem is formulated as a tilted coil above a horizontal interface. In that case, the full solution is a superposition of the fields produced by VMD and HMD sources. The FE and FD solutions are fully 3–D, since the numerical codes treat the problem as a horizontal coil above a dipping interface. The full 3–D physics of electromagnetic induction, including charge accumulation at the interface, is included in both formulations.

The physics of the problem is best investigated by analyzing the secondary magnetic field in the analytic coordinate system. The decomposition of the total response into the VMD and HMD fields reveals that the VMD produces horizontal loops of induced eddy currents which do not generate a charge accumulation. The HMD, however, produces a vertical component of induced eddy currents. Consequently, charge accumulation occurs as the eddy currents leak from the lower medium into the upper medium where the transmitter is located. The inductive and polarization effects seen in the real Z–signal are due to the secondary magnetic field caused by the eddy currents, combined with currents that arise to dissipate the charge buildup on the interface. These inductive and polarization effects often occur in induction logs in dipping geological formations.

In these calculations, it is advantageous to choose a background conductivity equal to that of the medium in which the transmitter is located. The reason for this choice is so that the secondary field are smoothly varying over the entire solution domain. If any other conductivity is selected to define the background medium, the secondary field will contain large gradients in the vicinity of the transmitter. A numerical code will experience difficulty capturing these large gradients accurately, so that the mesh would have to be made substantially finer.

Appendix: Finite Element Analysis

The Galerkin equations for the boundary value problem defined by Eq.(3–4), subject to homogeneous Dirichlet boundary conditions, are obtained by weighting Eq.(3) with the vector weighting functions $\mathbf{W}$, and Eq.(4) with the scalar weighting functions W. The weighting functions are satisfying:

$$\mathbf{W}\times\mathbf{n} = 0 \qquad W = 0 \qquad \text{on boundary}\,\Gamma \tag{A1}$$

since they are used in the expansion of $\mathbf{A_s}$ and Ψ_s. Hence:

$$\int_\Omega \mathbf{W}\cdot\nabla\times(\nabla\times\mathbf{A_s})\,d\Omega - \int_\Omega \mathbf{W}\cdot\nabla(\nabla\cdot\mathbf{A_s})\,d\Omega - j\omega\mu_0\int_\Omega \mathbf{W}\cdot(\sigma\mathbf{A_s})\,d\Omega - j\omega\mu_0\int_\Omega \mathbf{W}\cdot(\sigma\nabla\Psi_s)\,d\Omega =$$

$$= j\omega\mu_0\int_\Omega \mathbf{W}\cdot(\Delta\sigma\mathbf{A_p})\,d\Omega \tag{A2}$$

$$j\omega\mu_0\int_\Omega W\nabla\cdot(\sigma\mathbf{A_s} + \sigma\nabla\Psi_s)\,d\Omega = -j\omega\mu_0\int_\Omega W\nabla\cdot(\sigma\mathbf{A_p})\,d\Omega \tag{A3}$$

Integrating by parts in the first two volume integrals in Eq.(A2), and in the first volume integral in Eq.(A3) respectively, one obtains:

$$\int_\Omega \mathbf{W}\cdot\nabla\times(\nabla\times\mathbf{A_s})\,d\Omega = \int_\Omega(\nabla\times\mathbf{W})\cdot(\nabla\times\mathbf{A_s})\,d\Omega - \oint_\Gamma \mathbf{W}\cdot[(\nabla\times\mathbf{A_s})\times\mathbf{n}]\,d\Sigma \tag{A4}$$

$$-\int_\Omega \mathbf{W}\cdot\nabla(\nabla\cdot\mathbf{A_s})\,d\Omega = \int_\Omega(\nabla\cdot\mathbf{W})(\nabla\cdot\mathbf{A_s})\,d\Omega - \oint_\Gamma(\mathbf{W}\cdot\mathbf{n})(\nabla\cdot\mathbf{A_s})\,d\Sigma \tag{A5}$$

$$j\omega\mu_0\int_\Omega W\nabla\cdot(\sigma\mathbf{A_s} + \sigma\mathbf{A_p} + \sigma\nabla\Psi_s)\,d\Omega = j\omega\mu_0\oint_\Gamma W(\sigma\mathbf{A_s} + \sigma\mathbf{A_p} + \sigma\nabla\Psi_s)\cdot\mathbf{n}\,d\Sigma -$$

$$-j\omega\mu_0\int_\Omega(\nabla W)\cdot(\sigma\mathbf{A_s} + \sigma\mathbf{A_p} + \sigma\nabla\Psi_s)\,d\Omega \tag{A6}$$

The surface integrals in Eq.(A4) and Eq.(A6) vanish in view of Eq.(A1), while the one corresponding to Eq.(A5) vanishes due to $\nabla\cdot\mathbf{A_S}=0$ on Γ. Therefore, the Galerkin equations become:

$$\int_\Omega(\nabla\times\mathbf{W})\cdot(\nabla\times\mathbf{A_s})\,d\Omega + \int_\Omega(\nabla\cdot\mathbf{W})(\nabla\cdot\mathbf{A_s})\,d\Omega - j\omega\mu_0\int_\Omega\sigma(\mathbf{W}\cdot\mathbf{A_s})\,d\Omega -$$

$$-j\omega\mu_0\int_\Omega\sigma(\mathbf{W}\cdot\nabla\Psi_s)\,d\Omega = j\omega\mu_0\int_\Omega\Delta\sigma(\mathbf{W}\cdot\mathbf{A_p})\,d\Omega \tag{A7}$$

$$-j\omega\mu_0\int_\Omega\sigma(\nabla W)\cdot\mathbf{A_s}\,d\Omega - j\omega\mu_0\int_\Omega\sigma(\nabla W)\cdot(\nabla\Psi_s)\,d\Omega = j\omega\mu_0\int_\Omega\sigma(\nabla W)\cdot\mathbf{A_p}\,d\Omega \tag{A8}$$

By choosing $\mathbf{W} = N_i(x,y,z)\,\mathbf{u_x}$ and $W = 0$, where N_i –is the scalar shape function associated to node "i", Eq.(A7) transforms into:

$$\sum_k A_{s,k,x} \int_\Omega [(\nabla N_i)\cdot(\nabla N_k) - j\omega\mu_0\sigma N_i\, N_k]\, d\Omega + \sum_k A_{s,k,y} \int_\Omega (\nabla N_i \times \nabla N_k)\cdot\mathbf{u_z}\, d\Omega -$$

$$- \sum_k A_{s,k,z} \int_\Omega \int_\Omega (\nabla N_i \times \nabla N_k)\cdot\mathbf{u_y}\, d\Omega - \sum_k \Psi_{s,k} \int_\Omega j\omega\mu_0\sigma N_i \frac{\partial N_k}{\partial x}\, d\Omega =$$

$$= j\omega\mu_0 \sum_l \int_{\Omega_l} (\Delta\sigma)_l\, N_i\, A_{p,l,x}\, d\Omega_l \qquad (A9)$$

where:

$$A_{p,l,x} = \sum_{m=1}^{4} A_{p,(m,l),x}\, N_{(m,l)}(x,y,z) \qquad (A10)$$

and the summation is over all nodes "k" connected to node "i", and over all tetrahedra "l" to whom node "i" belongs.

Similar expressions are obtained when choosing $\mathbf{W} = N_i(x,y,z)\,\mathbf{u_y}$ and $W = 0$, or $\mathbf{W} = N_i(x,y,z)\,\mathbf{u_z}$ and $W = 0$ respectively:

$$- \sum_k A_{s,k,x} \int_\Omega (\nabla N_i \times \nabla N_k)\cdot\mathbf{u_z}\, d\Omega + \sum_k A_{s,k,y} \int_\Omega [(\nabla N_i)\cdot(\nabla N_k) - j\omega\mu_0\sigma N_i\, N_k]\, d\Omega +$$

$$+ \sum_k A_{s,k,z} \int_\Omega (\nabla N_i \times \nabla N_k)\cdot\mathbf{u_x}\, d\Omega - \sum_k \Psi_{s,k} \int_\Omega j\omega\mu_0\sigma N_i \frac{\partial N_k}{\partial y}\, d\Omega =$$

$$= j\omega\mu_0 \sum_l \int_{\Omega_l} (\Delta\sigma)_l\, N_i\, A_{p,l,y}\, d\Omega_l \qquad (A11)$$

with:

$$A_{p,l,y} = \sum_{m=1}^{4} A_{p,(m,l),y}\, N_{(m,l)}(x,y,z) \qquad (A12)$$

$$\sum_k A_{s,k,x} \int_\Omega (\nabla N_i \times \nabla N_k)\cdot\mathbf{u_y}\, d\Omega - \sum_k A_{s,k,y} \int_\Omega (\nabla N_i \times \nabla N_k)\cdot\mathbf{u_x}\, d\Omega +$$

$$+ \sum_k A_{s,k,z} \int_\Omega [(\nabla N_i)\cdot(\nabla N_k) - j\omega\mu_0\sigma N_i\, N_k]\, d\Omega - \sum_k \Psi_{s,k} \int_\Omega j\omega\mu_0\sigma N_i \frac{\partial N_k}{\partial z}\, d\Omega =$$

$$= j\omega\mu_0 \sum_l \int_{\Omega_l} (\Delta\sigma)_l\, N_i\, A_{p,l,z}\, d\Omega_l \qquad (A13)$$

with:

$$A_{p,l,z} = \sum_{m=1}^{4} A_{p,(m,l),z}\, N_{(m,l)}(x,y,z) \qquad (A14)$$

Finally, when choosing $\mathbf{W} = \mathbf{0}$ and $W = N_i(x,y,z)$, Eq.(A8) becomes:

$$-\sum_k A_{s,k,x} \int_\Omega j\omega\mu_0\sigma N_k \frac{\partial N_i}{\partial x}\, d\Omega - \sum_k A_{s,k,y} \int_\Omega j\omega\mu_0\sigma N_k \frac{\partial N_i}{\partial y}\, d\Omega - \sum_k A_{s,k,z} \int_\Omega j\omega\mu_0\sigma N_k \frac{\partial N_i}{\partial z}\, d\Omega -$$

$$-\sum_{k}\Psi_{s,k}\int_{\Omega} j\omega\mu_0\sigma\,(\nabla N_i)\cdot(\nabla N_k)\,d\Omega \;=\; j\omega\mu_0\sum_{l}\int_{\Omega_l}(\sigma)_l\left(\frac{\partial N_i}{\partial x}A_{p,l,x}+\frac{\partial N_i}{\partial y}A_{p,l,y}+\frac{\partial N_i}{\partial z}A_{p,l,z}\right)d\Omega_l \tag{A15}$$

where the Cartesian components of vector $\mathbf{A_{p,l}}$ are expressed by Eq.(A10), Eq.(A12) and Eq.(A14) respectively.

The group of Eq.(A9), Eq.(A11), Eq.(A13) and Eq.(A15) organized in a matrix form, define a symmetric algebraic system. The off–diagonal terms of the upper–left 3×3 part of the matrix, vanish on the interior of homogeneous subregions when conventional $C^0_{R^3}$ elements are used. This enhances the sparsity of the FE matrix. Indeed:

$$\int_{\Omega^e}(\nabla N_i\times\nabla N_k)\,d\Omega = \int_{\Omega^e}\left[\nabla\times(N_i\nabla N_k) - N_i\,(\nabla\times\nabla N_k)\right]d\Omega = \oint_{\Sigma^e}\mathbf{n}\times(N_i\nabla N_k)\,d\Sigma \tag{A16}$$

and since both N_i and the tangential derivatives of N_k are continuous at interior element boundaries, by proceeding with the summation over all elements, only the integrals on the exterior boundary may not cancel. This is due to the interior elements with common surfaces that share oppositely directed normals $\mathbf{n}$.

Regarding the terms associated to the fourth row and column corresponding to Eq.(A9), Eq.(A11), Eq.(A13) and Eq.(A15), it can be easily observed that:

$$a^{(i,k)}_{1,4} = -\int_{\Omega^e} j\omega\mu_0\sigma N_i\frac{\partial N_k}{\partial x}\,d\Omega = -\oint_{\Sigma^e} j\omega\mu_0\sigma N_i\,N_k\,n_x\,d\Sigma + a^{(i,k)}_{4,1} \tag{A17}$$

Similar expressions are obtained for $a^{(i,k)}_{2,4}$ and $a^{(i,k)}_{3,4}$. For the same reason as above when discussing Eq.(A16), by summing over all elements, the contributions given by $\oint_{\Sigma^e} j\omega\mu_0 N_i\,N_k\,\mathbf{n}\,d\Sigma$ cancel except eventually on the outer boundary. Therefore, $a^{(i,k)}_{m,4} = a^{(i,k)}_{4,m}$, $m\leq 3$, which concludes that the system matrix is a sparse and symmetric one.

Acknowledgment

Sections of this work were supported by the United States Department of Energy under contract DE-AC04-94AL85000. Sandia is a multiprogram laboratory operated by Sandia Corporation, a Lockheed Martin Company, for the United States Department of Energy.

References

[1] Barber, T.D., Howard, A.Q., "Correcting the Induction Log for Dip Effect", Society of Petroleum Engineers Paper 19607, 64–th Annual Technical Conference and Exhibition, San Antonio TX, pp.371–380, 1989.

[2] Howard, A.Q., Chew, W.C., "Electromagnetic Borehole Fields in a Layered, Dipping Bed Environment with Invasion", Geophysics, **57**, pp.451–465, 1992.

[3] Anderson, B., Barber, T.,Druskin, V., Lee, P., Dussan, E., Knizhnerman, L., Davydycheva, S., "The Response of Multiarray Induction Tools in Highly Dipping Formations with Invasion and in Arbitrary 3–D Geometries", SPWLA 37–th Annual Logging Symposium, Paper A, pp.1–14, 1996.

[4] Druskin, V., Knizhnerman, L., "Spectral Approach to Solving the Three Dimensional Maxwell's Diffusion Equations in the Time and Frequency Domains", Radio Sci., **29**, pp.937–953, 1994.

[5] Avdeev, D.B., Kuvshinov, A.V., Pankratov, O.V., Newman, G.A., Alumbaugh, D.L., "Modeling Induction Log Responses in Deviated Boreholes With Anisotropic Bedding", Geophysics, to appear, 2000.

[6] Hardman, R.H. and Shen, L.C., "Theory of Induction Sonde in Dipping Beds", Geophysics, **51**, pp.800–809, 1986.

[7] Biro, O., Preis K., "On the Use of the Magnetic Vector Potential in the Finite Element Analysis of Three–Dimensional Eddy–Currents", IEEE Trans. Magnetics, **25**, pp.3145–3159, 1989.

[8] Badea, E.A., Everett, M.E., Newman, G.A., Biro, O., "Finite Element Analysis of Controlled–Source Electromagnetic Induction Using Coulomb Gauged Potentials", Geophysics, to appear, 2000.

[9] Guptasarma, D., Singh B., "New Digital Filters for Hankel J_0 and J_1 Transforms", Geophys. Prosp., **45**, pp.745–762, 1997.

[10] Freund, R.W., Golub, G.H., Nachtigal, N.M., "Iterative Solutions of Linear Systems", in Iserles, A.(editor), Acta Numerica 1992, Cambridge Univ. Press, pp.57–100, 1992.

[11] Newman, G.A., Alumbaugh D.L., "Frequency–Domain Modelling of Airborne Electromagnetic Responses Using Staggered Finite Differences", Geophys. Prosp., **43**, pp.1021–1042, 1995.

[12] Liu, A., Joe, B., "Quality Local Refinement of Tetrahedral Meshes Based on 8 Subtetrahedron Subdivision", Mathematics of Computation, **65**, pp.1183–1200, 1996.

[13] Omeragic, D., Silvester P.P., "Numerical Differentiation in Magnetic Field Postprocessing", Int. J. Num. Modelling: Electronic Networks, Devices, Fields, **9**, pp.99–113, 1996.

Figure Captions

Figure 1. A y=0 slice in the vertical x/z–plane (top) and a z=0 slice in the horizontal x/y–plane (bottom) through a tetrahedral mesh containing two nested refinements. The actual meshes used to compute induction logging responses in this paper contain many more nodes than the mesh shown here, but the topology is the same. The heavy solid line in the upper figure corresponds to a bed boundary. Distances shown along the axes are in meters.

Figure 2. A horizontal coil embedded in a double halfspace conducting medium with a dipping interface. The electrical conductivity of the lower medium is σ_0 while that of the upper medium is σ_1. The center of the coil is located at depth h beneath the interface. The dip of the interface is α. Local mesh refinements were applied within the shaded rectangle.

Figure 3. Vertical cross–section in the x/z–plane through a small, but otherwise typical, finite element mesh. The heavy line is the interface between the two conducting media. Notice that the edges of tetrahedra conform simultaneously to the interface and the vertical axis.

Figure 4. The X and Z signal for various tilt angles. (a) X–signal, 30° tilt. (b) Z–signal, 30° tilt. (c) X–signal, 45° tilt. (d) Z–signal, 45° tilt. (e) X–signal, 60° tilt. (f) Z–signal, 60° tilt. The larger symbols represent the FE–computed solution, while the smaller symbols represent the Sandia FD–computed solution. The analytic Z–signals are shown as the lines without symbols.

Figure 5. Tetrahedron mean quality factor as a function of the tilt angle, for both refined and unrefined finite element meshes.

Figure 6. Schematic representation of the induced eddy current distribution caused by the VMD source located above the interface of two conducting media. The interface is shown in perspective by the heavy rectangle. The eddy currents are confined to horizontal loops.

Figure 7. (top) Schematic representation of the induced eddy current distribution caused by the HMD source located above the interface of two conducting media. The eddy and dissipative currents have both vertical and horizontal components, as shown in the bottom drawing.

Figure 8. Schematic representation of the electric charge accumulation generated by the HMD source. Two lobes of opposite polarity are located on the interface and generate dissipative currents. The symbol ρ_s refers to surface charge density.

Figure 9. Contours of the real Z–signal for the case of 45° dip, presented in the analytic

coordinate system. The coil axis is the dashed line.

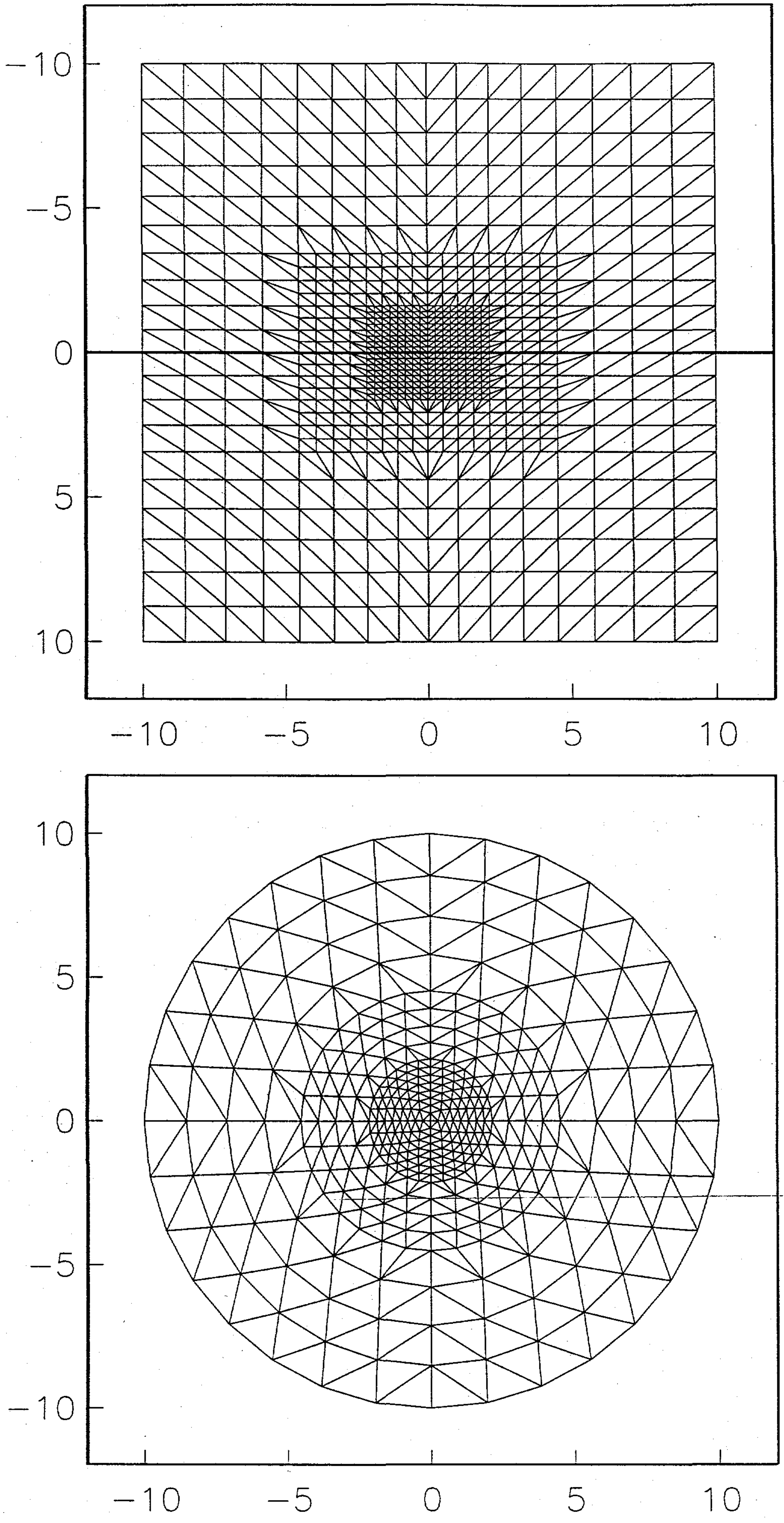

fig 1

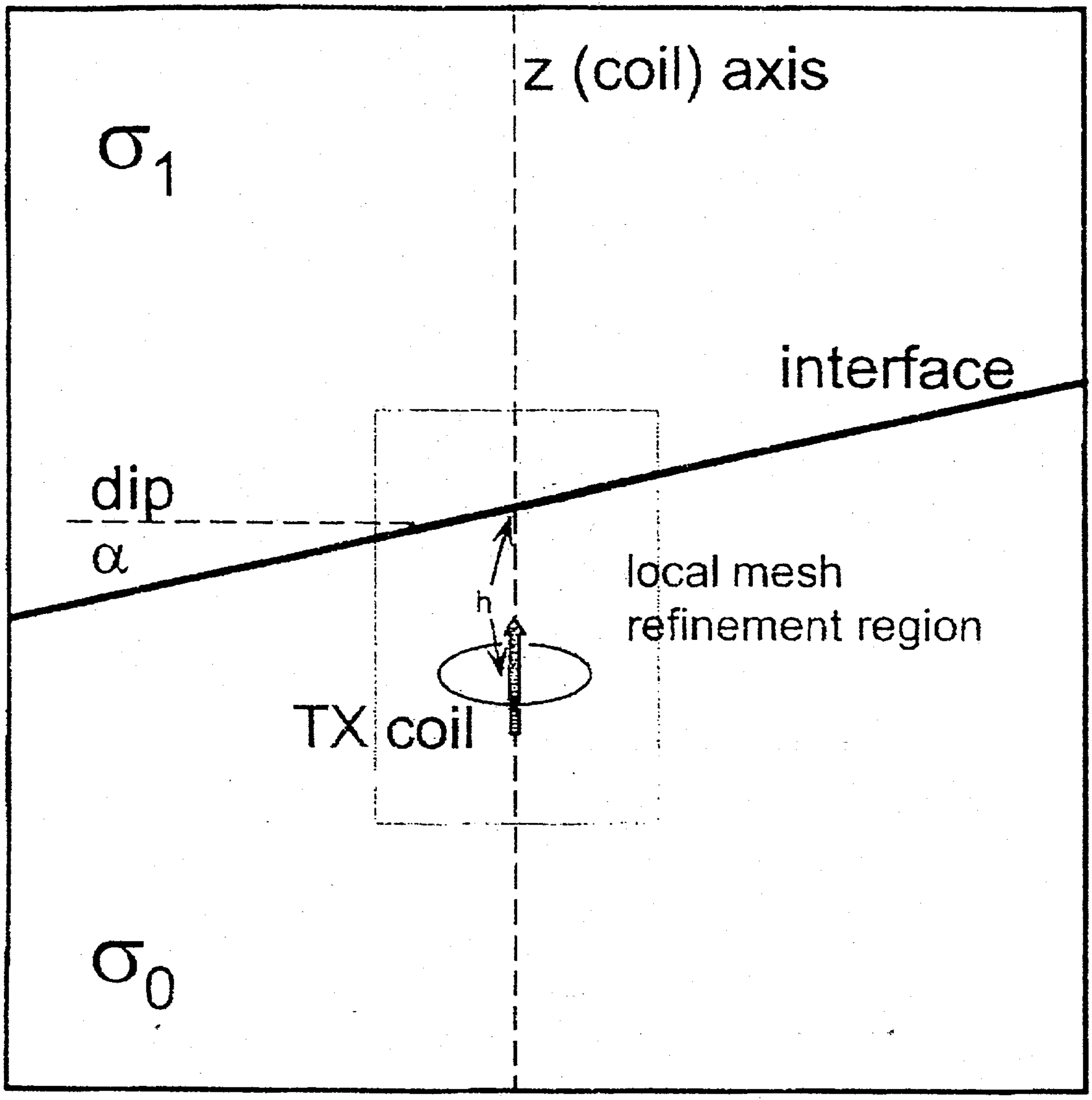
z (coil) axis
σ_1
interface
dip
α
h
local mesh
refinement region
TX coil
σ_0

Fig. 2

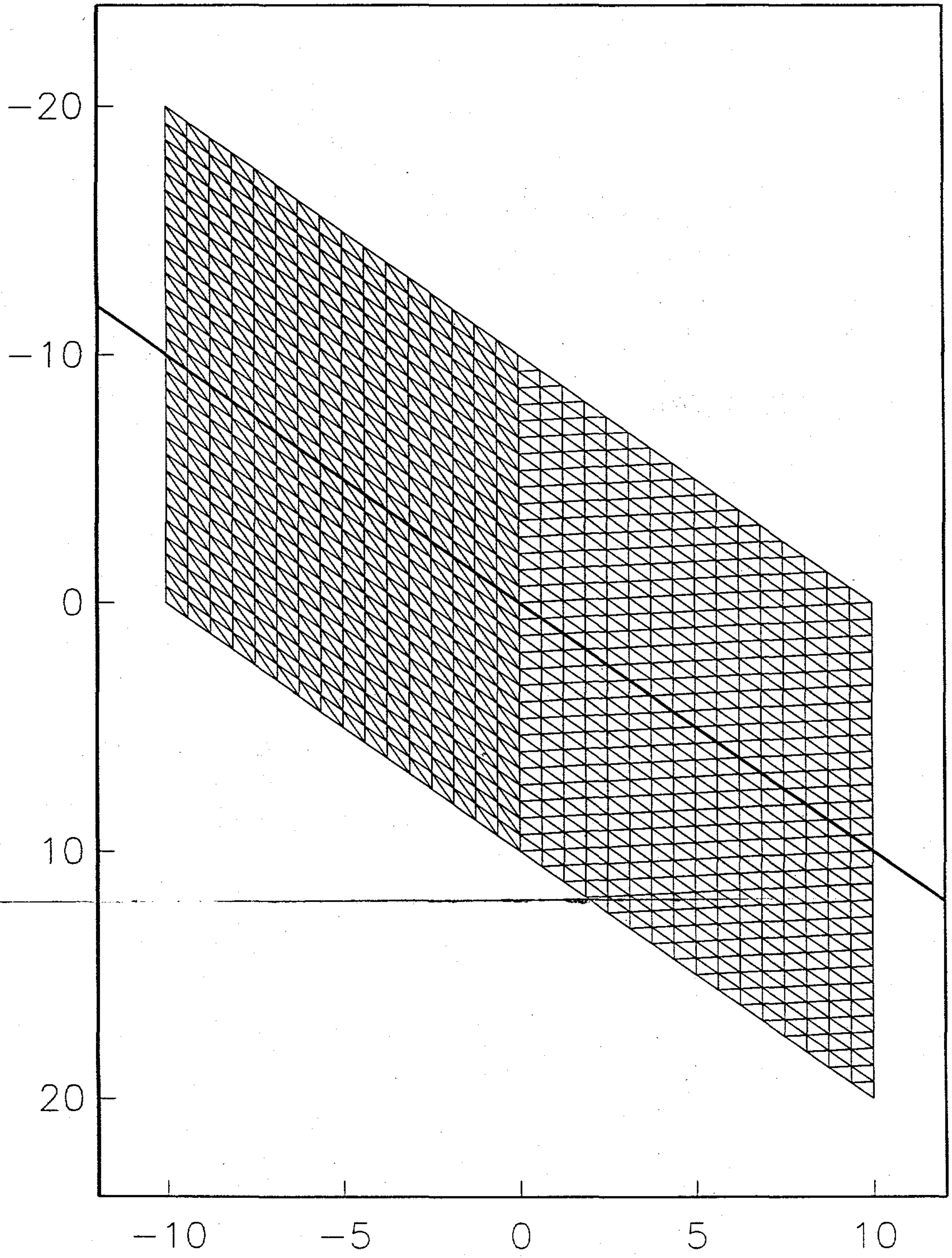

fig 3

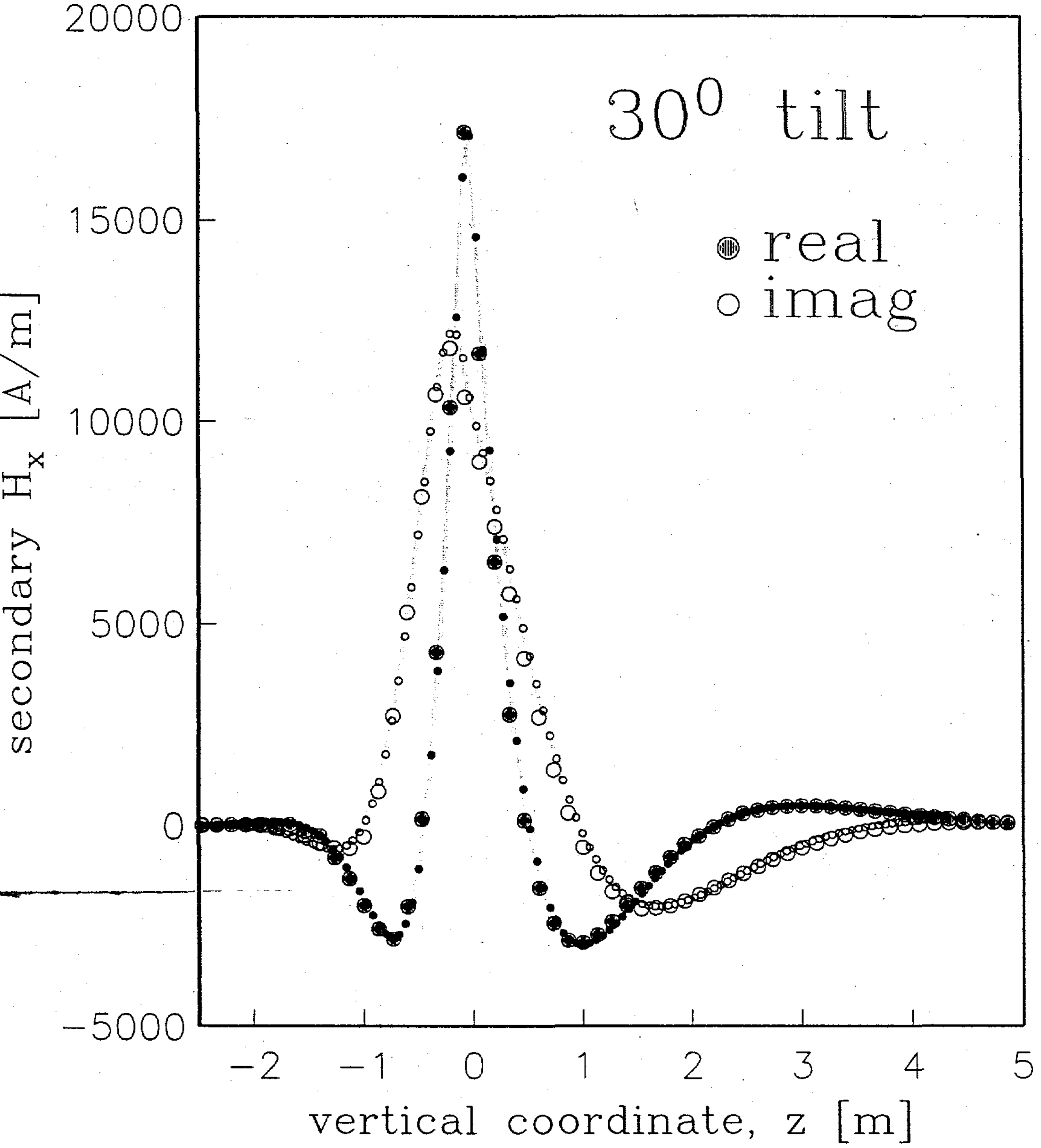

30^0 tilt
● real
○ imag
secondary H_x [A/m]
20000
15000
10000
5000
0
−5000
−2
−1
0
1
2
3
4
5
vertical coordinate, z [m]

fig 4a

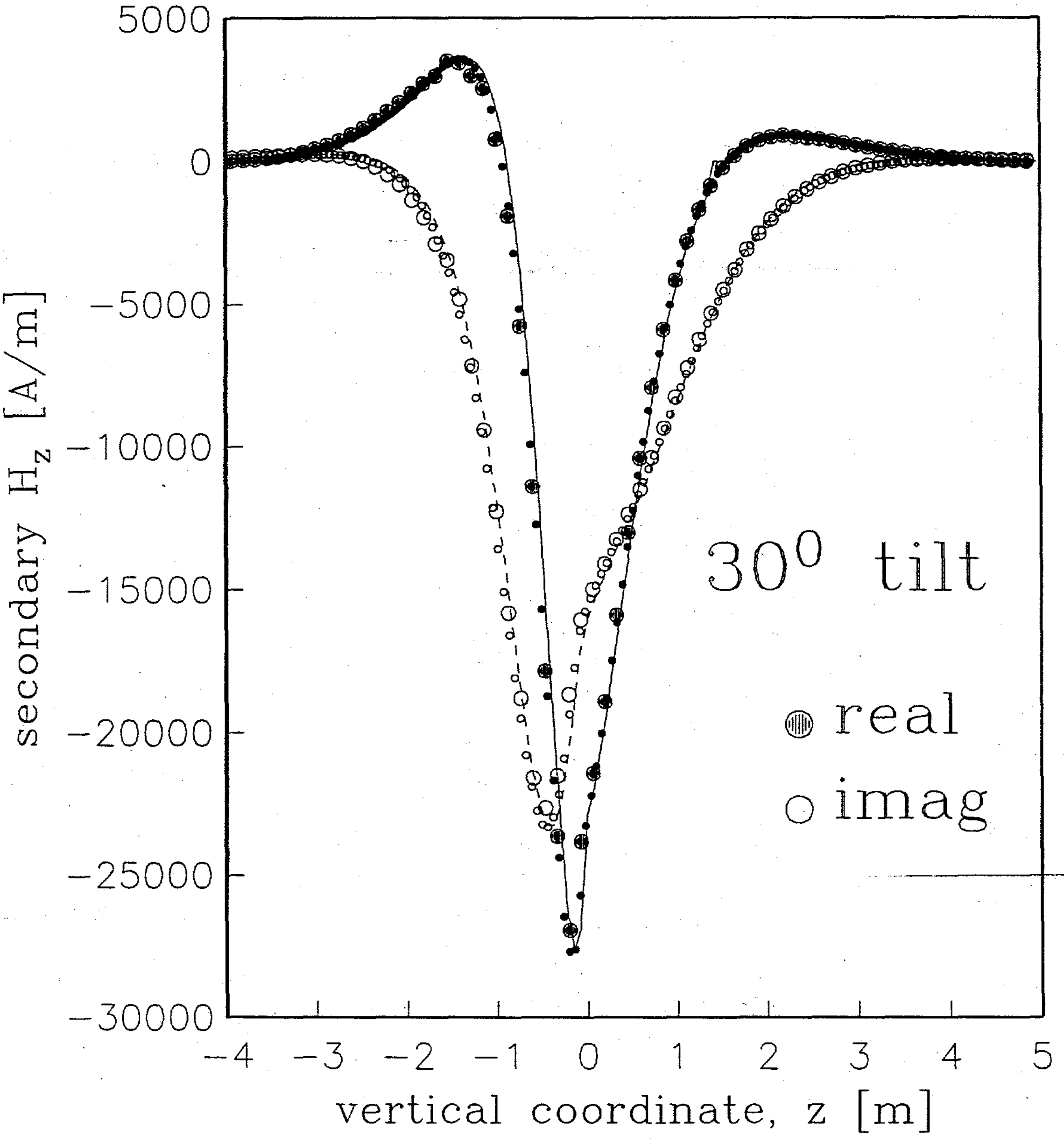
30⁰ tilt
real
imag
secondary H_z [A/m]
5000
0
−5000
−10000
−15000
−20000
−25000
−30000
−4
−3
−2
−1
0
1
2
3
4
5
vertical coordinate, z [m]

fig 4b

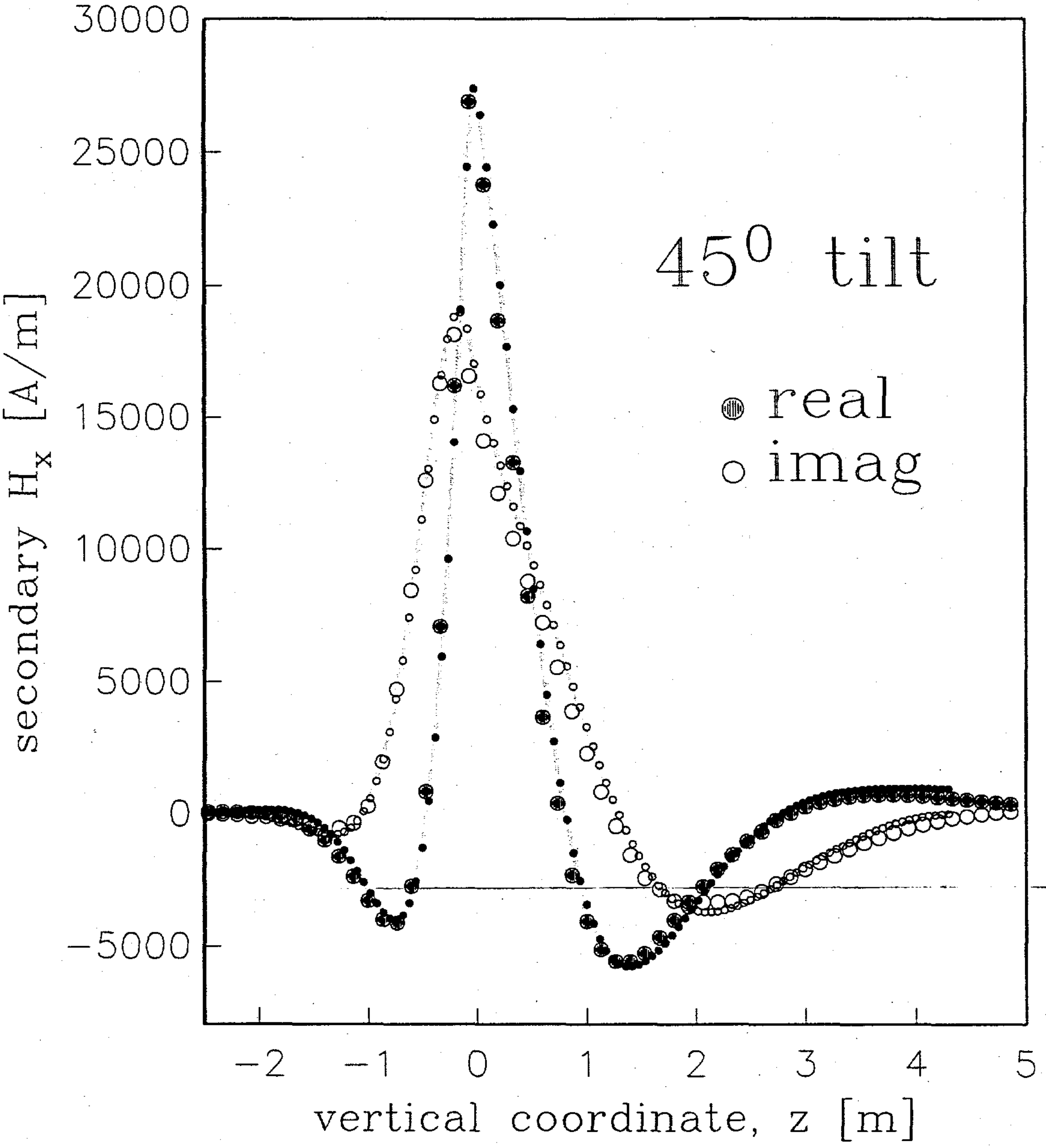
30000
25000
20000
15000
10000
5000
0
−5000
−2
−1
0
1
2
3
4
5
vertical coordinate, z [m]
secondary H_x [A/m]
45^0 tilt
● real
○ imag

fig 4c

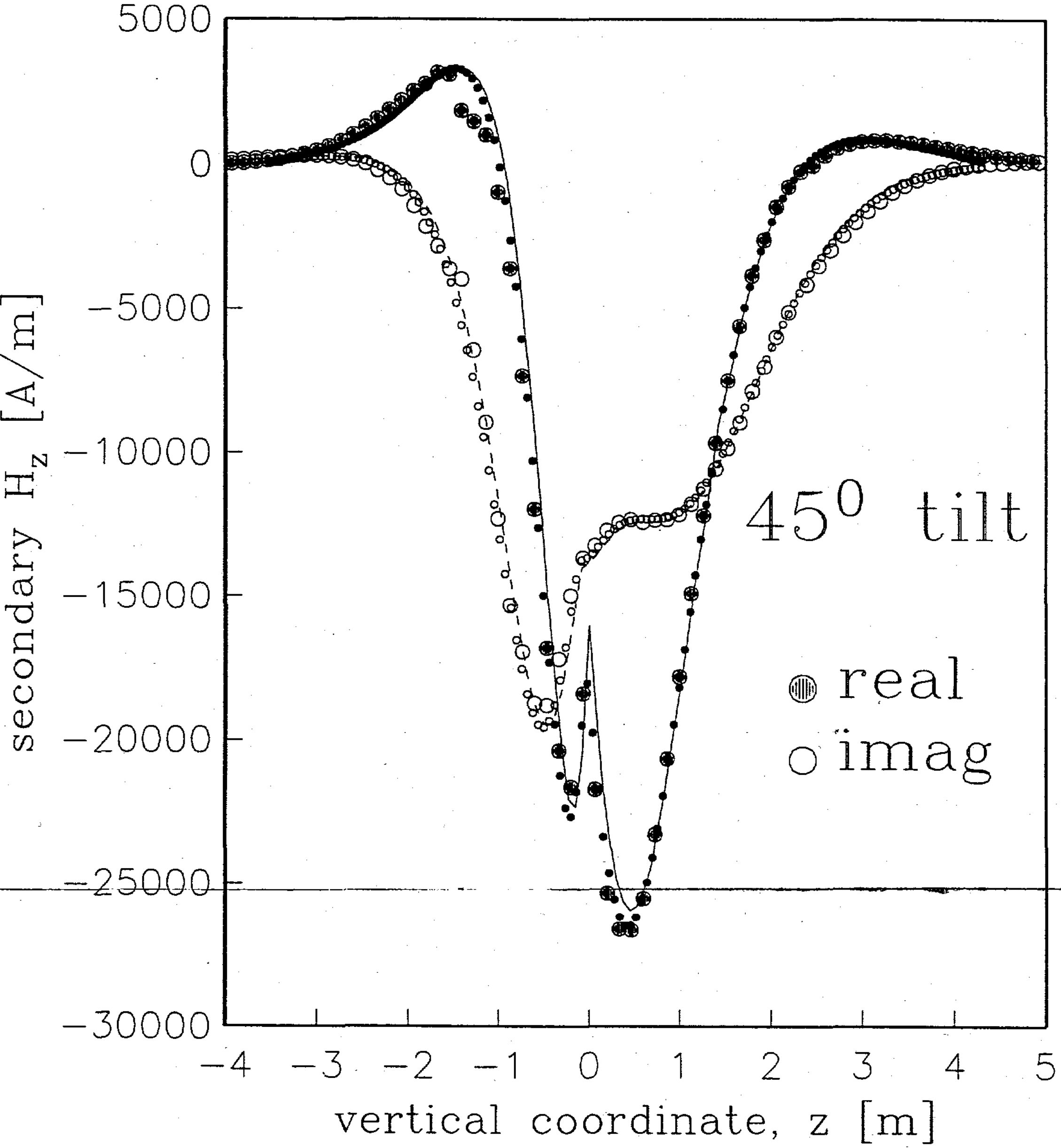
5000
0
−5000
−10000
−15000
−20000
−25000
−30000
secondary H_z [A/m]
−4
−3
−2
−1
0
1
2
3
4
5
vertical coordinate, z [m]
45^0 tilt
● real
○ imag

fig 4d

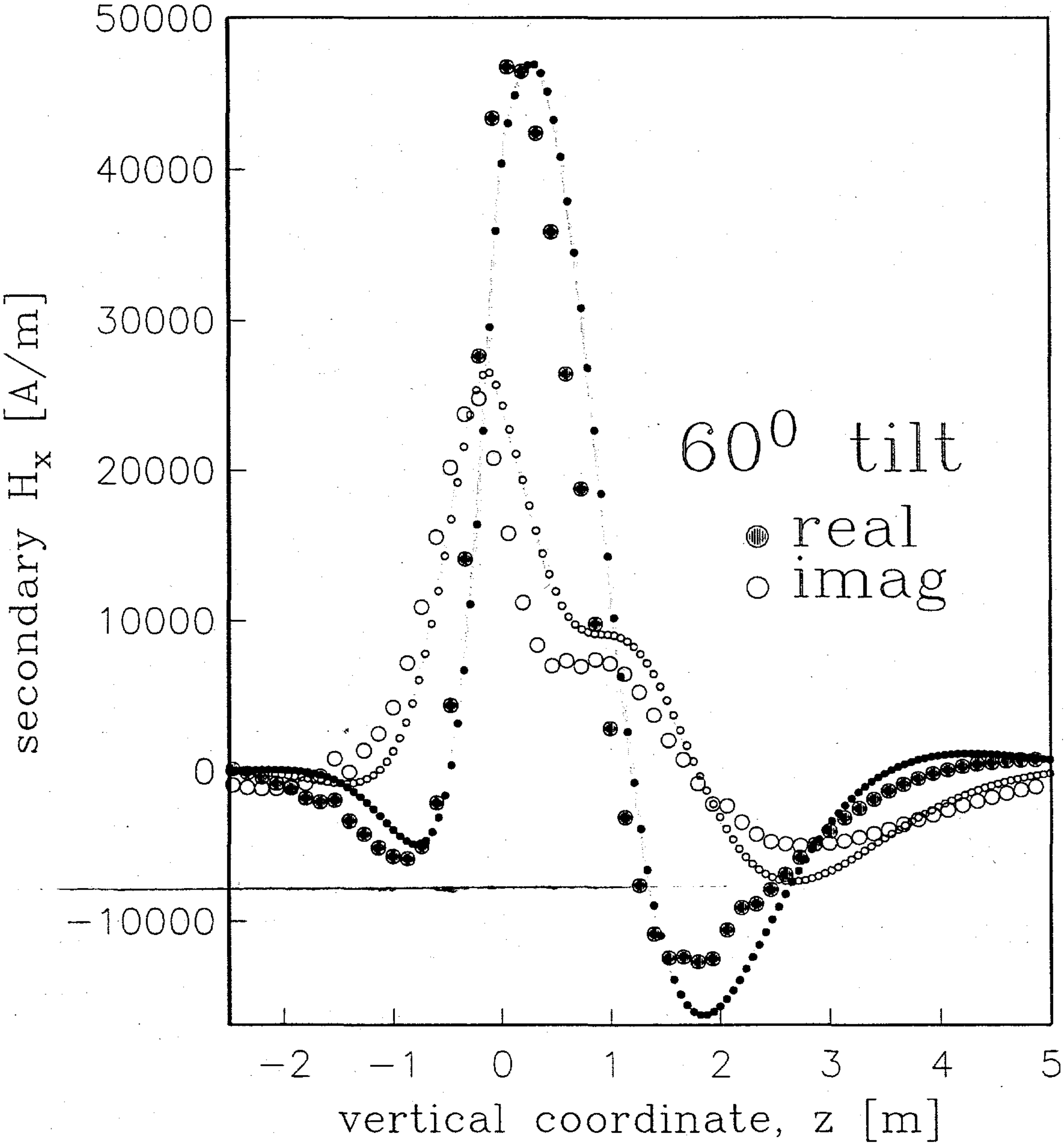

50000
40000
30000
20000
10000
0
−10000
secondary H_x [A/m]
−2
−1
0
1
2
3
4
5
vertical coordinate, z [m]
60⁰ tilt
● real
○ imag

fig 4e

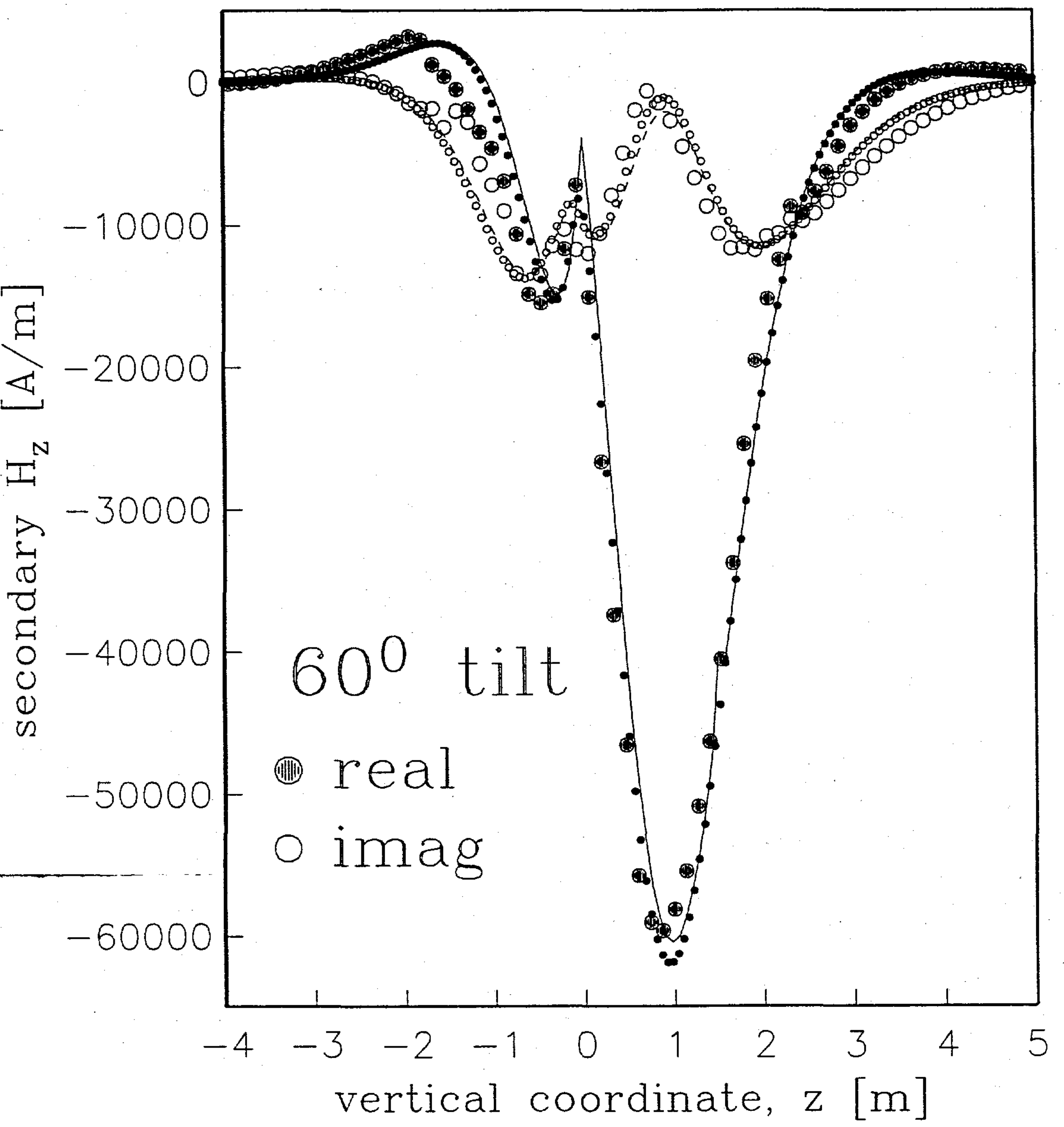
60^0 tilt
● real
○ imag
secondary H_z [A/m]
0
−10000
−20000
−30000
−40000
−50000
−60000
−4
−3
−2
−1
0
1
2
3
4
5
vertical coordinate, z [m]

fig 4f

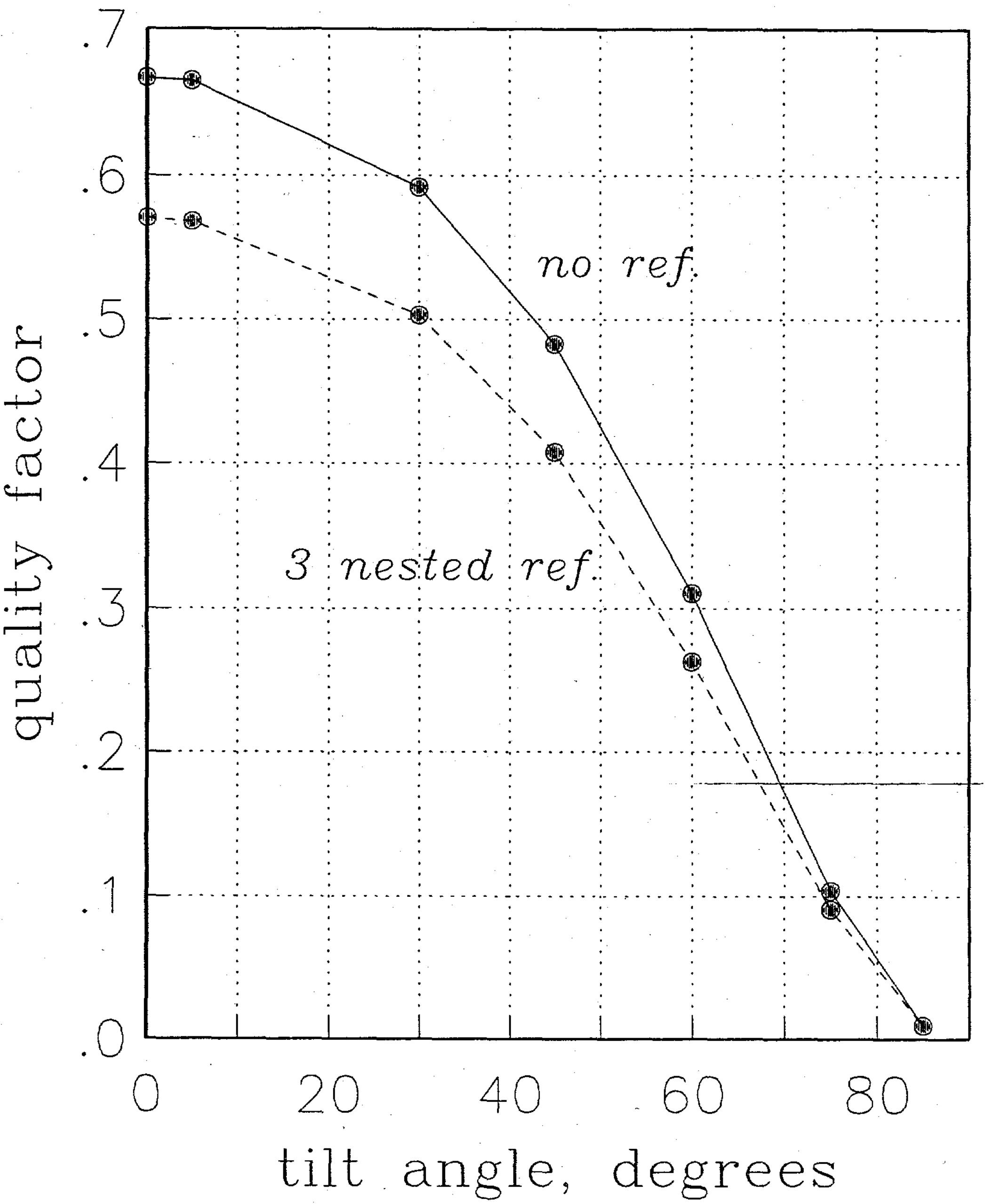
.7
.6
.5
.4
.3
.2
.1
.0
quality factor
0
20
40
60
80
tilt angle, degrees
no ref.
3 nested ref.

fig 5

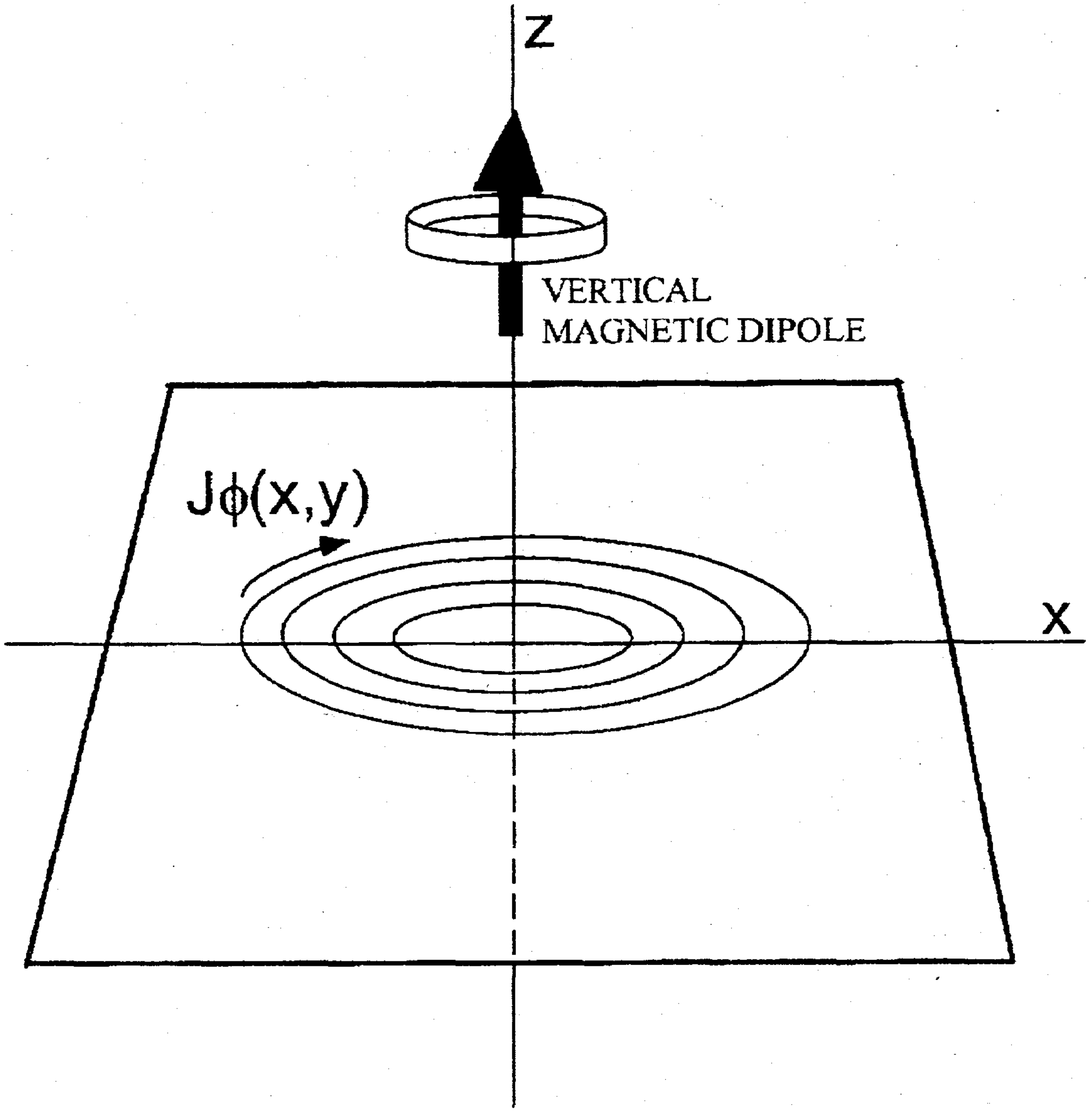
Z
VERTICAL
MAGNETIC DIPOLE
$J\phi(x,y)$
X

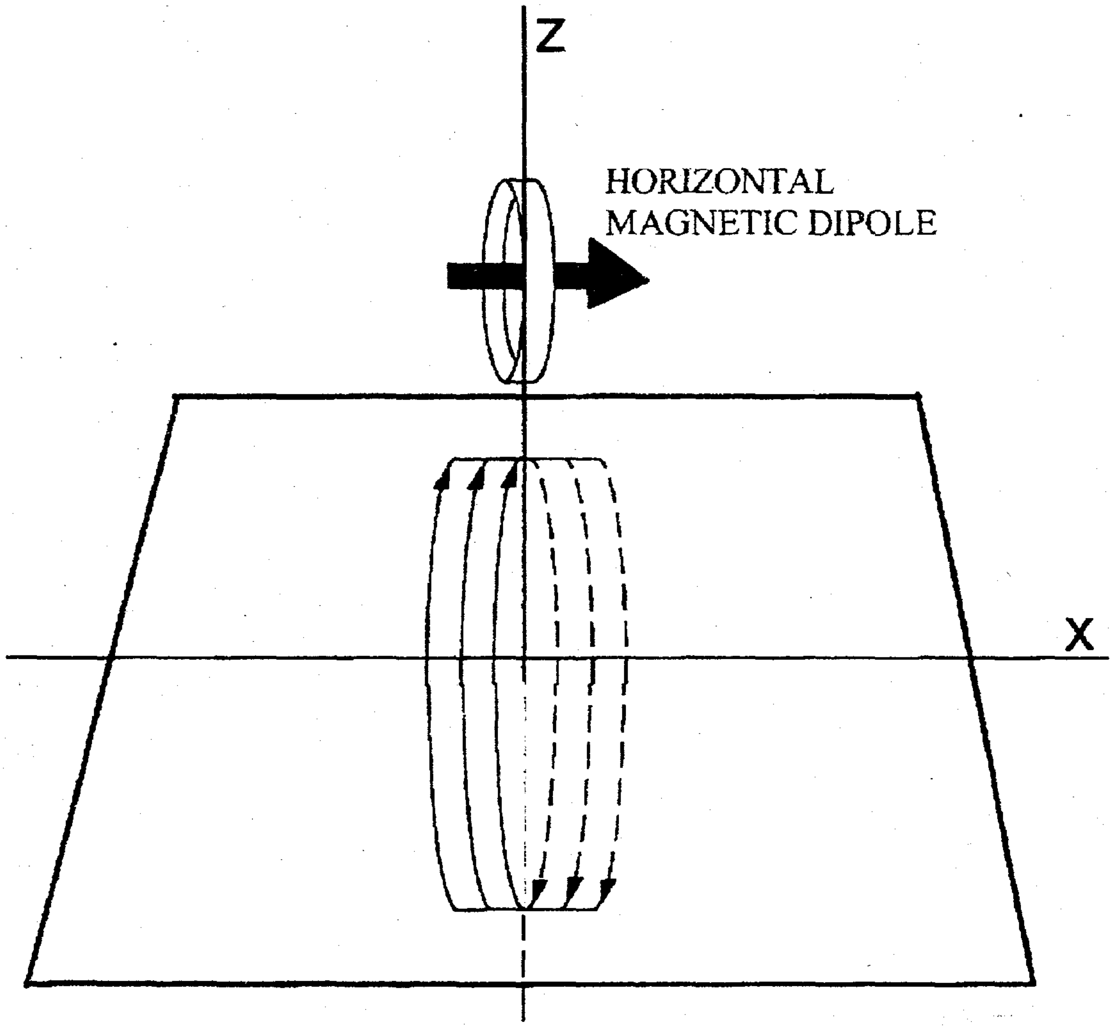

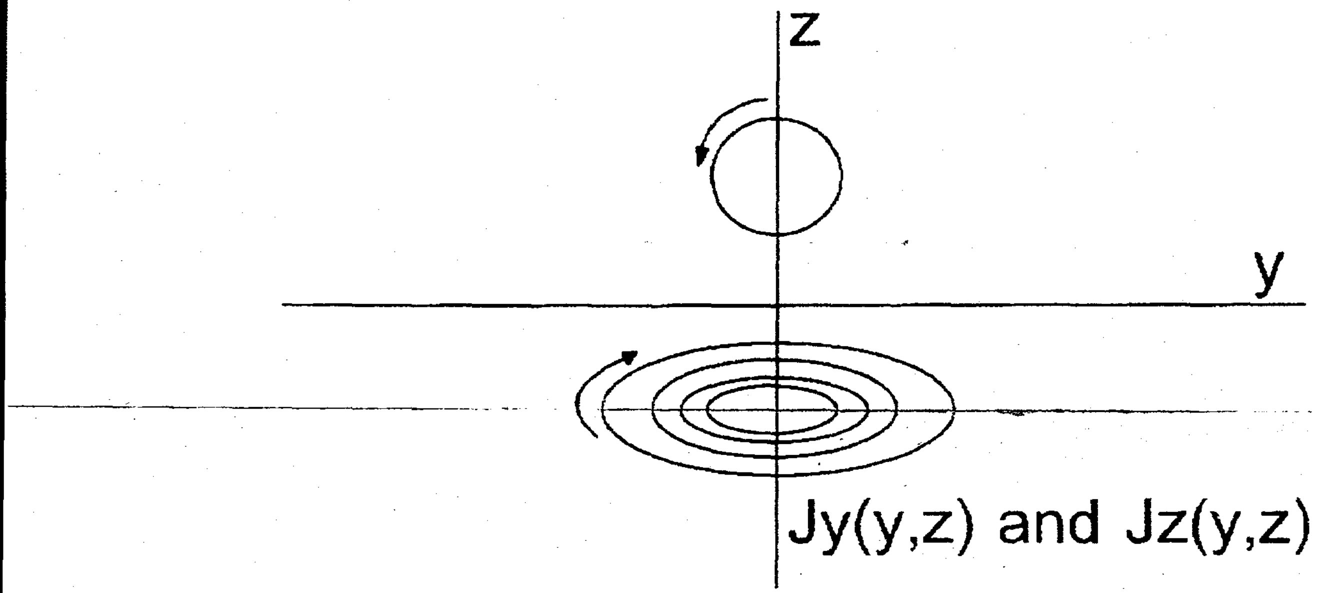

Jy(y,z) and Jz(y,z)

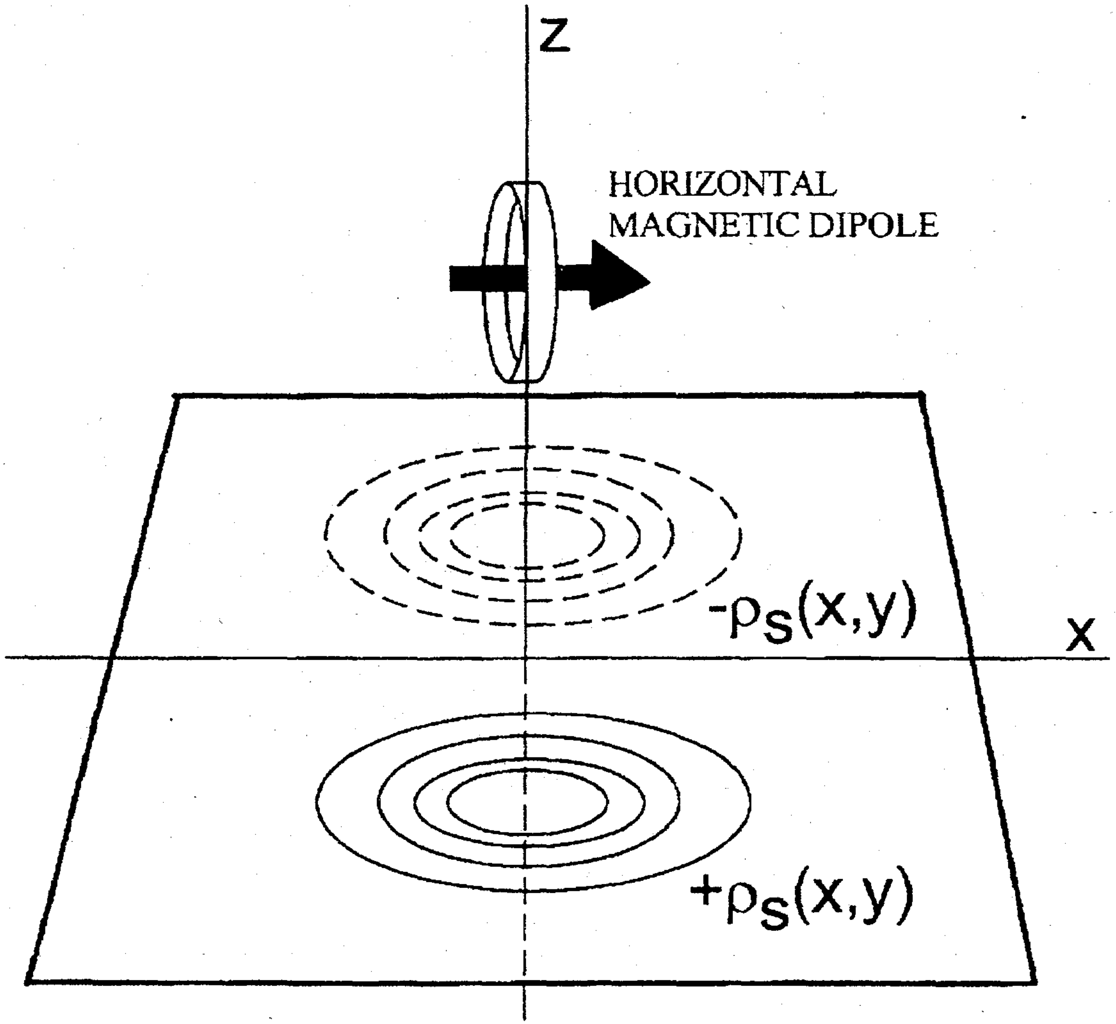

8

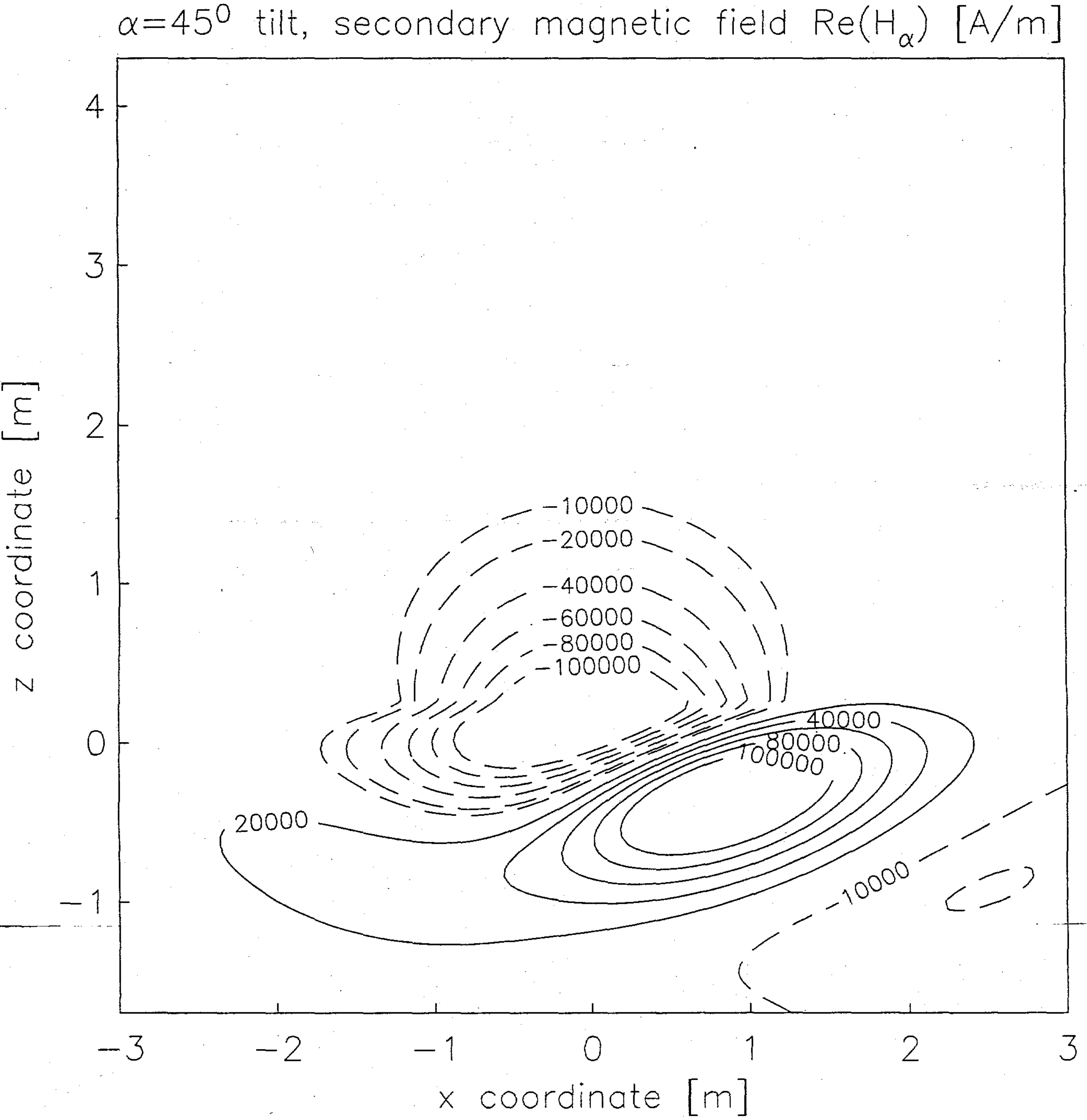

$\alpha=45^0$ tilt, secondary magnetic field $\mathrm{Re}(H_\alpha)$ [A/m]

fig9